Accepted Manuscript

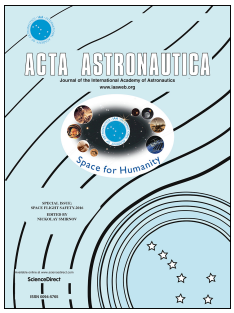

Performance of high mach number scramjets - Tunnel vs flight

Will O. Landsberg, Vincent Wheatley, Michael Smart, Ananthanarayanan Veeraragavan

PII: S0094-5765(17)31872-6

DOI: 10.1016/j.actaastro.2018.02.031

Reference: AA 6726

To appear in: *Acta Astronautica*

Received Date: 21 December 2017

Revised Date: 7 February 2018

Accepted Date: 21 February 2018

Please cite this article as: W.O. Landsberg, V. Wheatley, M. Smart, A. Veeraragavan, Performance of high mach number scramjets - Tunnel vs flight, *Acta Astronautica* (2018), doi: 10.1016/j.actaastro.2018.02.031.

68th International Astronautical Congress (IAC), Adelaide, Australia, 25-29 September 2017.

IAC–17–C4.9.16

PERFORMANCE OF HIGH MACH NUMBER SCRAMJETS - TUNNEL VS FLIGHT

Will O. Landsberg [a*], **Dr. Vincent Wheatley** [b]

Prof. Michael Smart[c], **Dr. Ananthanarayanan Veeraragavan**[d]

Centre for Hypersonics
The University of Queensland, Australia

While typically analysed through ground-based impulse facilities, scramjets experience significant heating loads in flight, raising engine wall temperatures and the fuel used to cool them beyond standard laboratory conditions. Hence, the present work numerically compares an access-to-space scramjet's performance at both these conditions. The Mach 12 Rectangular-to-Elliptical Shape-Transitioning scramjet flow path is examined via three-dimensional and chemically reacting Reynolds-averaged Navier-Stokes solutions. Flight operation is modelled through 800 K and 1800 K inlet and combustor walls respectively, while fuel is injected at both inlet- and combustor-based stations at 1000 K stagnation temperature. Room temperature walls and fuel plena model shock tunnel conditions. Mixing and combustion performance indicates that while flight conditions promote rapid mixing, high combustor temperatures inhibit the completion of reaction pathways, with reactant dissociation reducing chemical heat release by 16%. However, the heated walls in flight ensured 28% less energy was absorbed by the walls. While inlet fuel injection promotes robust burning of combustor-injected fuel, premature ignition upon the inlet in flight suggests these injectors should be moved further downstream. Coupled with counteracting differences in heat release and loss to the walls, the optimal engine design for flight may differ considerably from that which gives the best performance in the tunnel.

Keywords: Scramjet; Mach 12; Access-to-Space; Shock Tunnel; Flight Experiment

I 1. Introduction

While scramjets display improving technological readiness, financial constraints limit many researchers to ground-based impulse facilities [1] or numerical studies [2]. As Mach number increases, however, increased working pressures drive up the operational costs of reflected shock tunnels, while turbulent mixing between the driver and test gas interface reduces available test time [3]. These limitations have restricted the Mach number regime of flight tests, with the corresponding computational studies typically analysing mid-range Mach number ($5 \leq M < 10$) scramjets. These have included the Mach 5 X-51A [4], the Mach 7 X-43A [5] and the Mach 8 HyShot II [6] and HIFiRE 2 [7] experiments. While a small subset of ground-based studies examined high Mach number ($M \geq 10$) scramjets [8, 9], limited flight data exists for these engines. Restricted to the Mach 10 X-43A flight experiment [10], the significant expense and difficulty of high Mach number flight tests have driven the development of alternative tools to analyse steady scramjet operation. Computational fluid dynamics (CFD) is increasingly capable of fulfilling this role.

Simulations of mid-range Mach number flight experiments were subjected to extensive validation against shock tunnel data prior to the flight tests [11, 12]. Post-flight computational analysis displayed good agreement between the numerical studies and the steady flight data [13]. Further studies validated pre-flight predictions against flight data [10], supporting CFD's use as a scramjet design tool. As such, the opportunity exists to extend CFD's use to examine steady flight operation of high Mach number scramjets in the absence of experimental flight data.

Under flight conditions, wall surfaces encounter substantial thermal loads, with temperatures by necessity maintained near material thermal limits. Compared to cold-walled shock tunnel models, higher wall temperatures reduce energy loss through boundaries, while increasing the boundary layer thickness [14]. Active cooling measures are likely required to withstand these temperatures, with regenerative cooling using the fuel a likely candidate. This technology is in a mature state in rocket systems [15], and recently employed in the X-51 scramjet flight experiment [16]. It follows that injection of heated fuel will likely positively affect engine performance by reducing ignition delay, while mitigating system energy loss [17].

This paper compares flow-field differences and performance data of a scramjet operating within a shock tunnel environment, to one operating under steady flight. The Mach 12, Rectangular-to-Elliptical Shape-Transitioning (M12REST)

[a] PhD Candidate, w.landsberg@uq.edu.au
[b] Associate Professor, v.wheatley@uq.edu.au
[c] Professor, m.smart@uq.edu.au
[d] Senior Lecturer, anandv@uq.edu.au
* Corresponding Author

engine is examined as a case study. The REST inlet design methodology in [18] was tailored to a Mach 12 engine, before being refined through a series of studies [2, 8, 9, 17, 19]. The engine is a candidate for an access-to-space, accelerating engine when integrated to a hybrid rocket-scramjet-rocket launch vehicle [20]. However, no flight data for the high Mach number engine exists, nor have any numerical studies examined its steady-state flight operation. The work aims to provide a first numerical study to fill this gap.

II 2. Methodology

The internal flow path of the M12REST engine is shown in Fig. 1. The three-dimensional (3D) engine's lone symmetry-plane is about the centreline axis. Most recently examined in Landsberg et al. (2017) [2], an updated M12REST flow path is simulated here. The model is a geometric half scale of the original engine flow path, designed for Mach 12 flight at 50 kPa dynamic pressure. The engine has a total length of approximately 1275 mm, including a 500 mm forebody (omitted from Fig. 1), representative of the vehicle underside. The inlet is 476.2 mm in length, with a sidewall-to-sidewall capture width of 75 mm and becomes fully closed 339.6 mm downstream of the leading edge. The inlet achieves a geometric compression ratio of 6.61. 505.8 mm downstream of the inlet leading edge, shape-transition is complete with an elliptical aspect ratio of 1.76. The combustor begins following a short, 54.7 mm isolator. It maintains the same 430 mm^2 cross-section as the isolator and is inclined at 6° to the global streamwise direction, aligning the flow with the flight direction (the engine is inclined at 6° angle-of-attack). A conical nozzle terminates the engine, expanding the flow over 153.7 mm to a 10:1 area ratio relative to the engine throat [17]. The absence of a thrust-optimised nozzle ensures that reasonable comparisons of the flow path's thrust potential are beyond the scope of this work.

Hydrogen fuel is injected via inlet- and combustor-based stations. Inlet injection is achieved via three porthole injectors, 2 mm in diameter and inclined at 45° to the local wall normal. This injection location was chosen to maximise mixing length under shock tunnel conditions, providing a source of premixed fuel and radicals to accelerate combustion downstream, whilst ensuring substantial premature combustion induced pressure rise did not occur on the compression surface [8]. Combustor-based fuel injection is facilitated by 5 porthole injectors, located 470 mm from the leading edge. The centreline injector is $\oslash$1mm in diameter, while supplementary injectors are offset 45° and 70° from the symmetry plane and sized $\oslash$0.8mm and $\oslash$0.6mm respectively. All combustor-based injectors are inclined 30° to the local wall tangent vector, and the scheme takes advantage of *flow field manipulation*, as documented in [2].

II.i *2.1 Numerical Solver*

3D solutions to the compressible Reynolds-averaged Navier-Stokes (RANS) equations were computed using the research flow solver, US3D. Developed at the University of Minnesota [21], the solver is capable of solving structured, unstructured and hybrid meshes; however this investigation utilises structured meshes. US3D solves the RANS equations with a cell-centred finite volume scheme. A second-order, hybrid routine performs inviscid flux calculations. The solver uses the dissipative Stegar-Warming scheme in zones of large gradients and discontinuities [22], before swapping to a low dissipation scheme away from shocks and ensuring smooth transitions between each. Viscous fluxes are computed exactly using the MUSCL scheme on turbulent viscosity and conserved variables. Species-specific viscosity is determined through Blottner curve fits [23]. Solutions are generated using the implicit time marching Data-Parallel Point Relaxation method [24]. Turbulence was evaluated using the one equation, Spalart-Allmaras model [25], with initial turbulent viscosity set to be 3% of the Sutherland viscosity, default in US3D. For brevity, only the key numerical details of US3D are mentioned, and full details are given in [2, 21].

Scramjet flows with complex geometries have been previously simulated using US3D, with shocks, turbulence and non-equilibrium thermochemistry resolved [8]. Simulations of fuel injection into hypersonic cross-flows have been validated against temperature maps derived from nitric oxide planar laser-induced fluorescence measurements [26]. Turbulent variables were active from the forebody leading edge, with the turbulent Schmidt and Prandtl numbers set to 0.7 and 0.9 respectively. Prior simulations using these parameters have compared well to experimental data in the M12REST scramjet [8]. Solutions were run to converge the root-mean squared residual by at least 7 orders of magnitude, achieving domain mass balances of $\sum \dot{m} < 1 \times 10^{-8}$ kg/s. Thermally perfect gas behaviour was set, with temperature variant specific heat values taken from NASA Lewis data [27]. Finite-rate chemical reactions were modelled using the 13 species, 33 reaction hydrogen-air combustion mechanism of Jachimowski (1992) [28].

II.ii *2.2 Computational Meshes*

A structured mesh of the full engine flow path was generated, with smooth cell density blending from complex features such as leading edges and fuel injectors, to more coarsely discretised areas in the engine centre line. Cells were kept fine for approximately 30 jet diameters (D) downstream of fuel injectors. Viscous clustering was set to achieve a wall adjacent cell height of 0.7 μm across all wall boundaries, ensuring y^+ remained below one through the majority of the flow path. Where strong shock compression and stagnated flow interacted (i.e. the cowl closure notch),

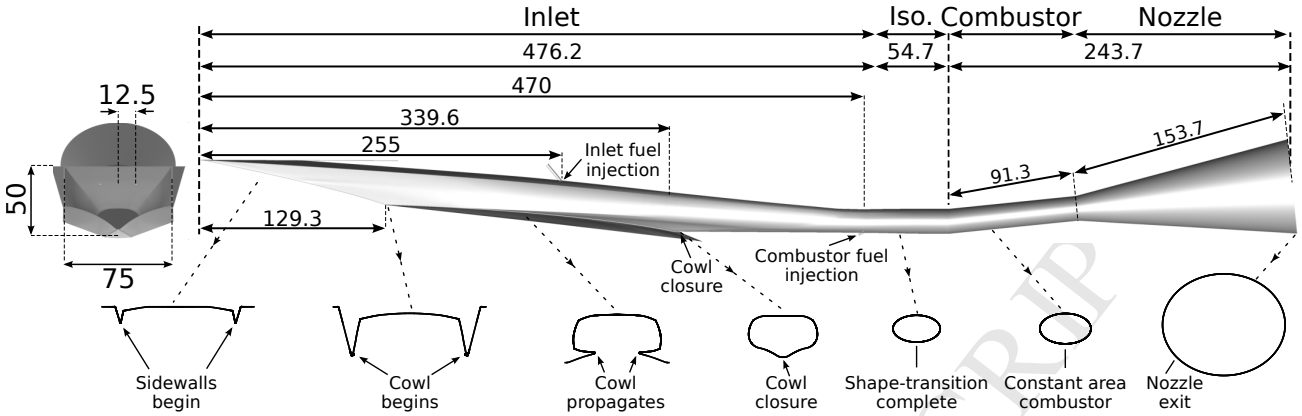

Fig. 1: Baseline M12REST flow path geometry: Front (left) and side (main) views [dimensions given in mm]

maintaining $y^+ < 1$ was not possible with the available resources. However, this zone only affected 0.008% of the inlet area and was assumed to have negligible impact on the solution.

To ensure grid independence, three computational models were examined: containing 9.9 million, 21.9 million and 42 million cells. All three meshes were run to convergence using the same inflow, fuelling and solver conditions, both for the shock tunnel and flight representative conditions. Convergence parameters included derived combustion and entrainment efficiencies (η_c, η_{ent}) and total combustion heat release ($\dot{H}$), as well as mass-weighted average properties of density ρ, temperature T, pressure p, and velocity U. While displaying convergent behaviour, the variables were not universally monotonic. For those variables displaying monotonic convergence, the recommendations of Stern at al. (2001) [29, 30] were followed with the calculated grid convergence indices suggesting that the finest grid should match the Richardson extrapolated value of an infinitely refined grid to within 0.2%. For those displaying oscillatory convergence, the method in [29] requires an additional solution. Using an additional 29.5 million cell mesh, all non-monotonically converging variables were estimated to be within 1.05% of an infinitely refined mesh, with the majority of variables converged to $< 0.8\%$. This non-monotonic behaviour is typical of hypersonic flows, where the solution order becomes linear in the presence of shocks [31]. As such, the solutions provided by the finest grid are assumed to be grid independent, and are hence utilised in the remainder of the present work.

III 3. Tunnel vs Flight - Flow & Model Conditions

Model inflow conditions were based on those produced in the University of Queensland's, T4 Stalker tube reflected shock tunnel. Experimental validation of the M12REST flow path was performed by Wise (2015) [9], with conditions set to match Mach 12 flight. These conditions assumed the inlet was integrated to the vehicle forebody and inclined at 6° to the flight path angle; however an additional 1.6° angle-of-attack was given to the experimental model and numerical inflow to ensure the incoming Mach number matched the on-design conditions. The properties in Table 1 were developed using UQ's in-house code, NENZFr, which expands the nozzle supply pressure through T4's Mach 10 nozzle geometry in thermochemical non-equilibrium using a 5 species finite-rate air chemistry model [32]. As little flow stagnation occurs in flight, flight simulation species mass fractions were set based on a 3.76/1 by mole fraction N_2/O_2 atmosphere. Remaining fluid properties were left unchanged, allowing direct comparisons to be made.

Table 1: Freestream inflow conditions

Parameter	Shock tunnel	Flight representative	Equivalent flight
M	9.183	9.183	11.75
H, MJ/kg	7.01	7.01	7.01
U, m/s	3630	3630	3678
T, K	386.8	386.8	243.71
ρ, g/m^3	10.51	10.51	5.69
p, Pa	1177	1177	398.7
q, kPa	69.23	69.23	38.55
Y_{N_2}	0.7285	0.767	0.767
Y_{O_2}	0.1837	0.233	0.233
Y_{NO}	0.08273	0	0
Y_O	0.005102	0	0
Altitude, km	-	-	37.38

To model shock tunnel research, non-slip, 300 K isothermal wall boundaries were imposed, as millisecond-scale test times result in negligible temperature increases. While previous studies analysing steady flight operation have used adiabatic walls [12], it is expected that combustion chamber temperatures experienced in Mach 12 flight would exceed typical material thermal limits. With this noted, flight forebody and inlet wall temperatures were set to be isothermal at 800 K, which has been demonstrated to not induce

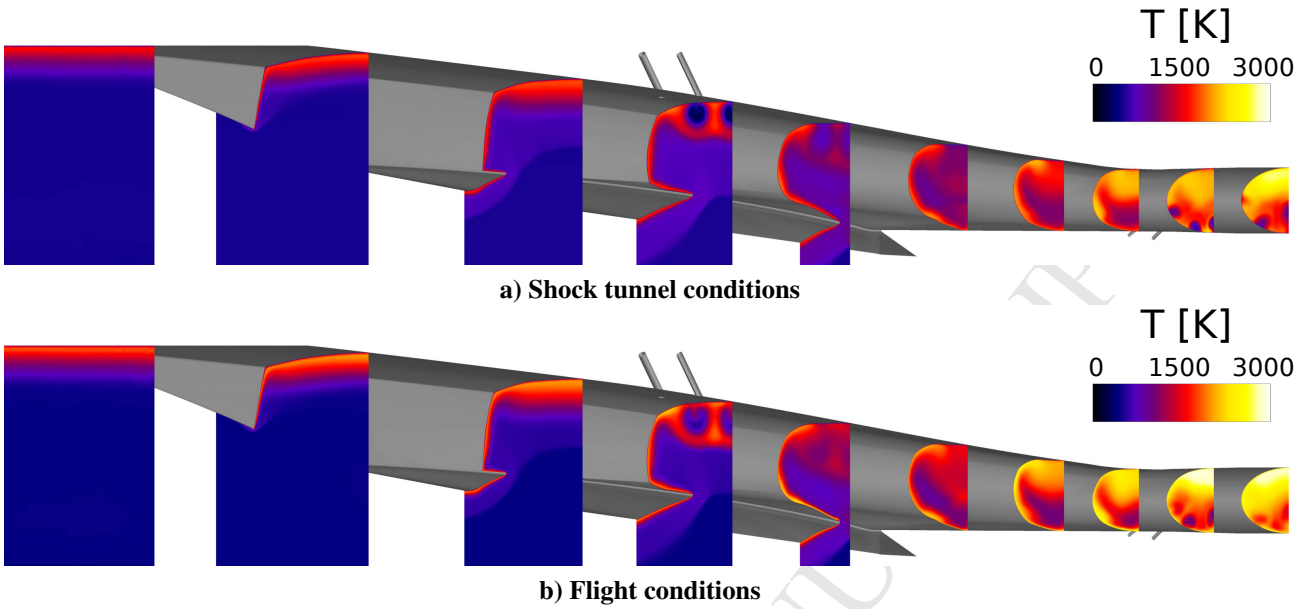

Fig. 2: Inlet temperature contours

premature combustion of intake injected fuel [33]. Downstream of the cowl closure, wall temperature is ramped in proportion to the inlet area contraction to reach 1800 K by the combustor entrance, holding these combustor and nozzle walls at the upper operational limit of ceramic matrix composites such as carbon fibre reinforced silicon carbide (C/C-SiC) [34].

Fuel injection is facilitated by both inlet- and combustor-based injectors. Previous experimental and numerical validations have shown good performance injecting hydrogen at a 30/70 ratio of inlet/combustor injectors, for a total equivalence ratio of $\phi = 1.26$ [17]. This fuelling ratio is maintained in the flight case, requiring 21% more fuel due to the absence of inflow NO which reduces the oxygen available for combustion under shock tunnel conditions. Shock tunnel fuel injection velocity and temperature were assumed sonic, corresponding to isentropic expansion from 300 K stagnation conditions. Under flight conditions, it is assumed the fuel is used as the primary regenerative coolant, being heated from cryogenic liquid to 1000 K. This corresponds to proposed coolant exit temperatures in the literature which reference values 890-1050 K [35, 36], with it assumed that Mach 12 flight would require the maximum cooling capacity available. To heat liquid hydrogen to these conditions would require 14.53 MJ/kg [37], providing approximately 31 kW of full-engine cooling capacity under flight-level fuelling rates. Future studies can consider this using full conjugate heat transfer [38], once the exact requirements of the cooling of the hot surfaces are better understood. As previously, fuel injection velocity and temperature were determined using isentropic expansion to sonic conditions, this time from 1000 K stagnation temperature. Fuelling rates are given in Table 2, with rates given for engine half-plane which was simulated. All subsequent references to fuelling rates and combustion heat release are given for the engine half-plane.

Table 2: Fuelling conditions

Parameter	Shock Tunnel Case		Flight Case	
	$\dot{m}$, g/s	ϕ	$\dot{m}$, g/s	ϕ
Total	1.749	1.26	2.112	1.26
Inlet-based	0.503	0.36	0.607	0.36
Combustor-based	1.246	0.90	1.505	0.90

IV 4. Results & Discussion

IV.i *4.1 Flow Field Contours*

Contours of temperature through the inlet are given in Fig. 2. The beginning of the inlet is quasi-two-dimensional, with the thick boundary layer developed over the vehicle forebody evident in each case. Immediately, prior to the inlet-based fuel injectors, the boundary layer has thickened to 12.3 mm in the flight conditions (FL) case, increasing by 10% when compared to the 11.2 mm encountered in the shock tunnel (ST) case. This boundary layer thickening is expected for models with heated walls [14]. To examine fuel jet penetration, the total vertical displacement of the fuel jet from the bodyside wall at the cowl closure location is examined, setting the penetration limit at the location where the hydrogen fuel reaches the stoichiometric hydrogen-air combustion mass fraction. The thickened boundary layer combines with the increased dynamic pressure of the heated fuel jet [17] to increase fuel penetration to 13.2 mm, by

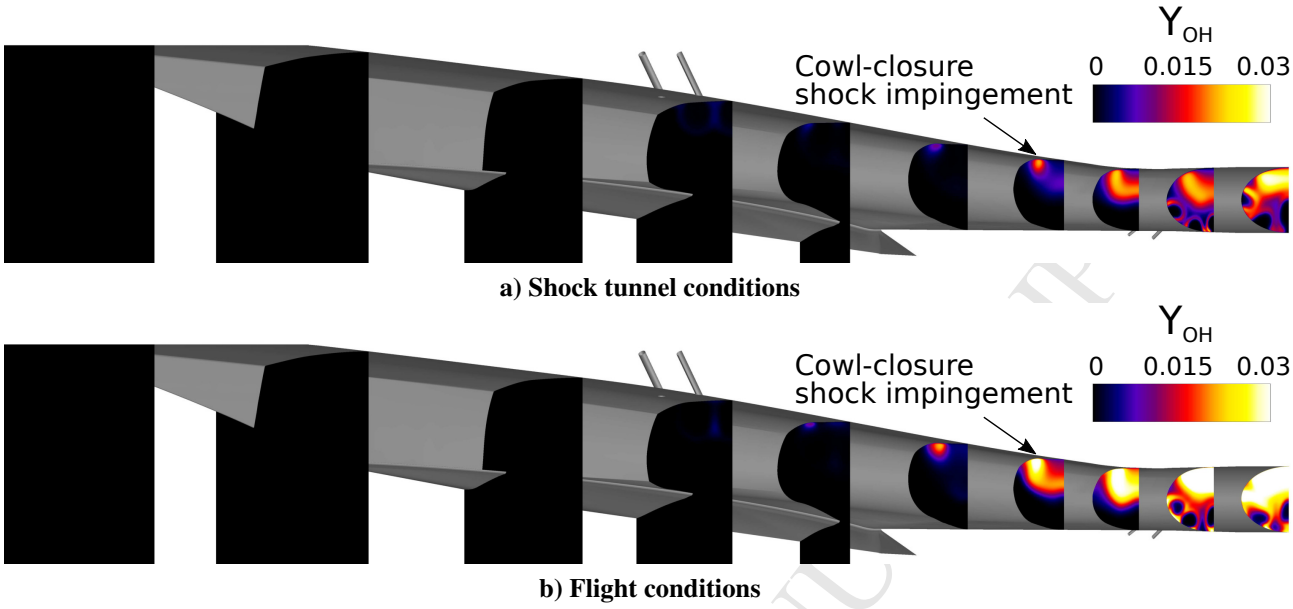

Fig. 3: Inlet hydroxyl radical (OH) contours

cowl closure, compared to the 10.5 mm achieved by the ST case. This increased jet penetration for the FL case is evident in Fig. 2b, with the jets expanding to a greater extent than those in the ST case in the slice immediately downstream of the inlet-based fuel injectors. The heated walls further influence the flow, with the reduced heat loss ensuring the mass-weighted temperature and pressure at the combustor entrance reach 1910 K and 105 kPa respectively. This represents increases from the ST case of 13% and 47% for temperature and pressure respectively, with the ST case only reaching 1690 K and 71.2 kPa. As temperature and pressure tend to dominate ignition characteristics, the hydroxyl radical (OH, indicative of hydrogen ignition in air) is examined in Fig. 3.

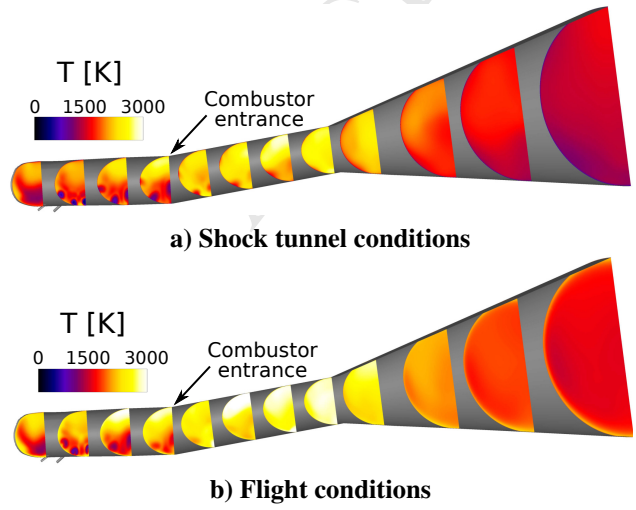

Fig. 4: Combustor temperature contours

In each case, no OH radicals are observed outside of the bodyside boundary layer flow prior to combustor-based fuel injection, confirming the observations in prior work [8]. It is not until additional fuel is injected further downstream that the cowlside core flow of air is able to mix and react with fuel. While prior works examining different scramjet geometries have indicated that little ignition of inlet-injected fuel occurs prior to the combustor [33], the strong cowl closure shock impinges on the fuel-rich, bodyside boundary layer and ignites the fuel. Under shock tunnel conditions, this ignition process induces marginal drag increases, while providing a source of premixed fuel and combustion radicals to pilot combustion of fuel injected further downstream [8]. Under flight conditions however, this influence is more substantial. As shown in Fig. 3, the ignition of fuel occurs further upstream than the cowl closure shock impingement location, with its subsequent impingement inciting robust combustion and OH radical formation. While previous works have concluded that only marginal OH formation occurs within a scramjet whose inlet temperature reaches up to 700K [39], in these studies, the hydrogen fuel penetrated well beyond the high temperature, boundary layer. As the inlet fuel injectors in the M12REST engine do not in fact penetrate through this bodyside boundary layer, the high temperatures experienced therein may accelerate the combustion processes, with the reduced ignition delay promoting premature ignition. Hence, this may indicate that the inlet fuel injectors should be moved further downstream when the scramjet is operating under flight-representative conditions, ensuring the degree of combustion upon the compression surface is reduced. The combustor and nozzle temper-

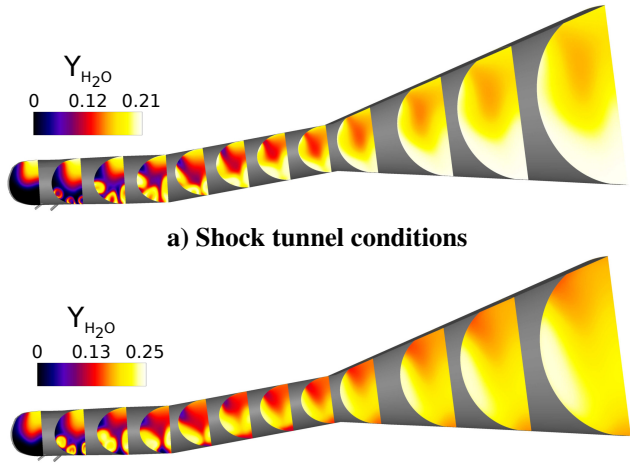

Fig. 5: Combustor water (H_2O) contours

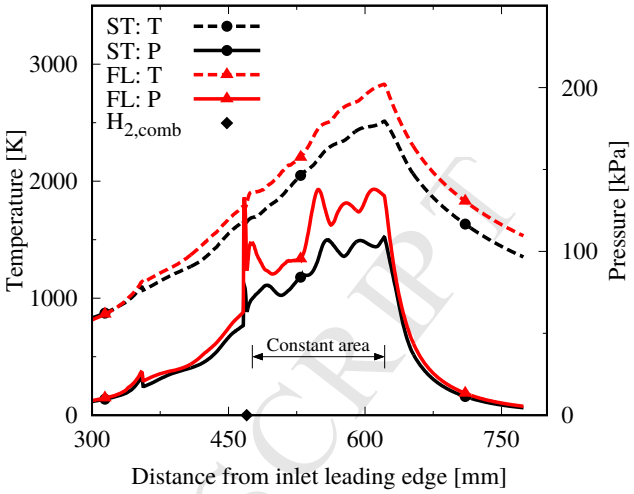

Fig. 6: Average streamwise temperature and pressure

ature contours are hence shown in Fig. 4.

The FL case experiences increased temperature throughout the isolator and combustor. This is not unexpected, however the extent to which it increases is of note. At locations of shock impingement, localised regions of gas exceed 3000 K, while by the combustor exit the entire cross-section approaches this limit. This greatly exceeds the 2500 K threshold indicated by Kutschenreuter (2000) [40], at which the obtainable net combustion heat release begins to rapidly diminish. By comparison, the ST case maintains more reasonable temperatures within the 2000-2500 K range. While OH is indicative of ignition and combustion, combustion radicals must be permitted to recombine to H_2O to complete the H_2-O_2 reaction process and ensure all available heat of combustion is delivered to the flow [41]. Hence, contours of H_2O are shown in Fig. 5.

When examining water vapour contours, it is important to note that the inflow conditions govern the final water mass fraction which would be achieved should the mixture reach chemical and diffusive equilibrium. Under flight conditions, with a 3.76/1, N_2/O_2 atmosphere and hydrogen fuel injection at ϕ =1.26, complete combustion with chemical and diffusive equilibrium would yield $Y_{H_2O} \approx 0.25$. Under shock tunnel conditions, the facility reflected shock dissociates some of the test flow, which is then chemically frozen as it expands through the facility nozzle and over the experimental model. Hence, the oxidisers are O_2 and O, while oxygen contained within NO is assumed to be lost to the reaction pathways. Hence, using the mass fractions of the oxidisers given in Table. 1, the equilibrium water content is $Y_{H_2O} \approx 0.21$. Shown in Fig. 5, the ST case achieves a greater relative proportion of H_2O than the FL case as the flow expands through the engine nozzle. This indicates that the flow conditions in the ST case are more conducive to the final recombination reactions, permitting the H_2-O_2 combustion process to proceed to completion.

IV.ii *4.2 Average Flow Properties*

It is hypothesised that high temperatures within the FL combustor and nozzle are preventing recombination of combustion products. To examine this quantitatively, the mass-weighted average temperature and pressure for each case are given in Fig. 6, with the location of combustor-based fuel injection ($H_{2,comb}$) also indicated.

As previously indicated, prior studies have indicated that significant performance losses are incurred when H_2-O_2 combustion temperatures exceed 2500 K [40]. The ST case reaches this threshold only momentarily before the temperature relaxes as it expands through the nozzle, and the combustor mean temperature remains at 2330 K. The FL case, however, exceeds this limit for approximately 80 mm (4.6 combustor heights, h_{comb}), from the station at 560 mm to the station at 640 mm. With a peak combustor temperature of 2830 K and combustor mean temperature of 2591 K, significant reductions in total extractable heat are to be expected. Examining pressure, the FL case exceeds the ST case throughout the entire combustor, with a mean of 127 kPa (compared to 100 kPa for the ST case). While higher pressures will increase combustion rates, system efficiency will reduce. Smart (2012) [42] determined that ideal scramjet performance is attained when combustor entry pressure remains at approximately 50 kPa. With each case's mean combustor pressure exceeding this limit, performance improvements may be attained with a lower contraction ratio inlet. The necessary contraction ratio reduction would be amplified for a scramjet operating in steady flight; however it is noted that a full scale engine would be used in flight, and the larger size would likely affect the combustor entrance conditions.

IV.iii *4.3 Mixing & Combustion Performance*

Mixing and combustion performance under both shock tunnel and flight conditions are examined. The RANS simulations performed do not track scalar variance, and hence the time-averaged solution is used to calculate a macroscopic entrainment efficiency, η_{ent}, in place of a 'mixing' efficiency [43]. This is determined by taking the ratio of mixed oxygen[b] (the limiting reactant for the fuel-rich simulations performed), to the total oxygen present. The set of equations is shown in Eq. (1) and (2), with integrals performed over cross-planes at streamwise locations x.

$$\eta_{\text{ent}}(x) = \frac{\dot{m}_{\text{O}_2,\text{mix}}\,(x)}{\dot{m}_{\text{O}_2,\text{total}}\,(x)} = \frac{\int Y_{\text{R}}\rho U dA}{\int Y_{\text{O}_2}\rho U dA}, \tag{1}$$

$$Y_{\text{R}} = \begin{cases} Y_{\text{O}_2} & \text{if } Y_{\text{O}_2} \leq Y_{\text{O}_2,\text{stoich}} \\ Y_{\text{O}_2,\text{stoich}}\frac{1-Y_{\text{O}_2}}{1-Y_{\text{O}_2,\text{stoich}}} & \text{if } Y_{\text{O}_2} > Y_{\text{O}_2,\text{stoich}} \end{cases} \tag{2}$$

This set of inequalities evaluates the mass fraction of oxygen contained within each cell, in each streamwise-plane, and if it is less than that necessary to achieve stoichiometric combustion with the hydrogen present in that cell (i.e. at fuel-rich conditions), the full mass fraction of oxygen within that cell is considered *mixed*. If the cell is fuel-lean however, the mass fraction of oxygen necessary to react stoichiometrically with the available hydrogen is determined. This new value of oxygen is, by definition, less than the total oxygen present within that cell. This calculation is performed for each cell in the current plane, and the ratio between the integrated values of mixed and total oxygen mass flow rates represents the entrainment efficiency, as in Eq. (1).

For the fuel-rich simulations performed, combustion efficiency refers to the ratio of oxygen-mass which is fully reacted to completion (i.e. present in H_2O), and the total oxygen captured by the inlet. This is shown in Eq. (3).

$$\eta_{\text{c}}(x) = \frac{0.8881\dot{m}_{\text{H}_2\text{O}}}{\dot{m}_{\text{O}_2,\text{total}}}, \tag{3}$$

In both entrainment and combustion efficiency calculations, nitrogen bound species (e.g. NO) are excluded from the calculations as it is deemed inaccessible to hydrogen-based reactions [17]. Efficiencies are shown varying with streamwise distance from the inlet leading edge in Fig. 7. The locations of inlet-based ($H_{2,\text{inlet}}$) and combustor-based fuel injection ($H_{2,\text{comb}}$) are also indicated.

The FL case achieves a greater degree of mixing throughout the entire domain. By the nozzle outflow plane, the FL case achieves 99.6%, compared to 98.0% for the ST case. While only a marginal increase, the FL case exceeds 80% mixing efficiency prior to the combustion chamber entrance, whereas the ST case requires an additional $1.2h_{\text{comb}}$ to reach parity. This reduction in mixing length may permit a shorter combustion chamber, or reduced inlet-fuelling ratio for flight operation.

[b] Mixed refers to the mass flow rate of O_2 which would react with the available hydrogen under infinitely fast chemistry conditions.

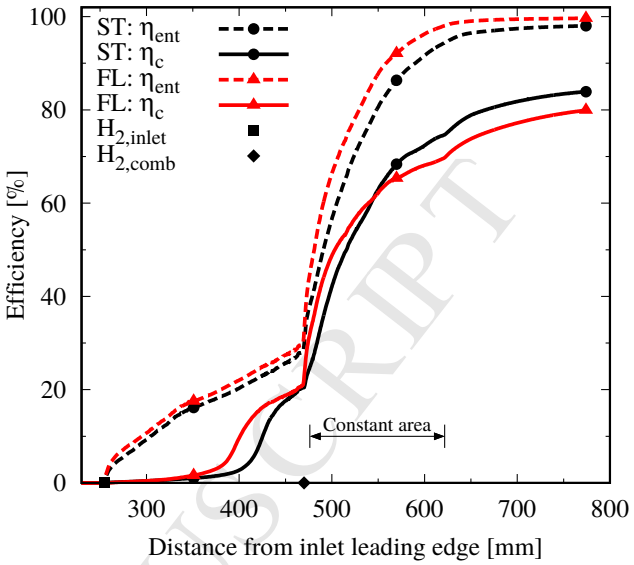

Fig. 7: Entrainment and combustion efficiency

Combustion performance does not follow these trends. While the freestream radicals in shock tunnel conditions may accelerate ignition of fuel, the radical-free flow in the FL case initially achieves a greater degree of combustion. However, this drops below the ST case just $1h_{\text{comb}}$ downstream of the combustor entrance. The ST case hence achieved 80% combustion efficiency (the nominal threshold proposed by Smart [42] to achieve net thrust during flight) $6.2h_{\text{comb}}$ upstream of the nozzle exit, while the FL case only achieves 79.9% at the nozzle exit. This phenomena is likely due to high combustor and nozzle temperatures dissociating the flow and preventing the reactions from proceeding to completion, restricting the production of H_2O.

IV.iv *4.4 Combustion Heat Release*

While combustion efficiency is conventionally used to analyse engine performance, energy addition to the flow is the primary goal of combustion. Heat release to the flow may be analysed by summing the product of species formation rates (w_{s}, units kg/[s·m^3]) and their corresponding enthalpies of formation (ΔH_{f}, J/kg). When performed for each species present in the Jachimowski (1992) hydrogen-air reaction mechanism [28], the summation of each cell's local value across streamwise slices gives the instantaneous heat release rate through the flow path in kW/m, which may be integrated through the flow path to determine the cumulative heat release (in kW), as shown in Fig. 8.

$$\dot{H} = \sum_{i}^{\text{n}} \left(w_{\text{s},i} \times \Delta H_{\text{f},i}\right), \tag{4}$$

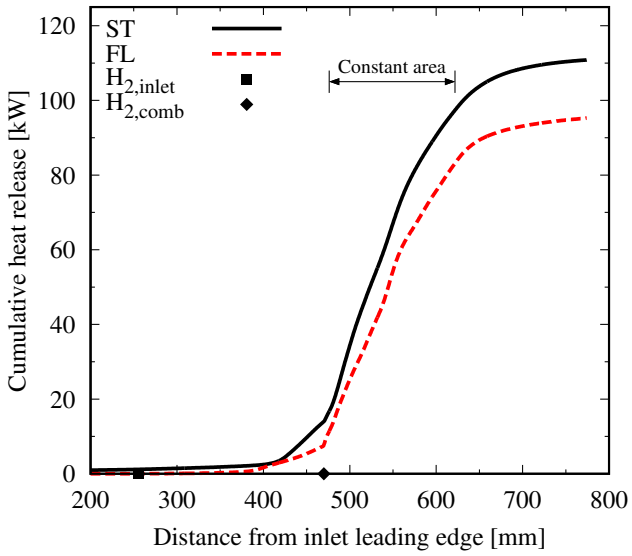

Fig. 8: Cumulative heat release

The ST case reaches 111 kW by the engine exit plane, displaying markedly increased heat release over the FL case which achieved 95 kW. This reduced heat release is likely due to the reduced recombination of combustion radicals to the final products, combining with the combustor temperatures which exceeded 2500 K [40]. To examine this, species-specific cumulative heat release (or absorption in the case of negative values) are given in Fig. 9. These are given for species for which the net heat release/absorption exceeds 1 mW, and are specific to the Jachimowski (1992) [28] combustion mechanism utilised in this study.

While the H_2O-specific heat release for the FL case exceeds that achieved for the ST case, the greater proportion of heat absorbed by the atomic hydrogen and oxygen combustion products ensure that the total heat release is curtailed below that achieved by the ST case. It is noted that, with no freestream oxygen contained in NO and the increased fulling rate required, the FL case would be expected to release more heat to the flow. As this is not achieved, it indicates that the flow path geometry and/or fuelling schemes must be altered to improve operation under steady-flight.

IV.v *4.5 Heat Loads*

While achieving improvements in system performance under flight representative conditions, the heated walls are expected to experience significantly reduced heat transfer. Integrated heat loads for the full internal flow path for both unfuelled and fuelled, ST and FL cases are hence presented in Table 3. It is noted however that the FL case wall temperature was set based upon the fuelled flow path, and hence the unfuelled FL case is not expected to reach the same temperatures. As such, the unfuelled FL case was set to maintain wall temperatures of 800 K throughout the entire flow path. The fuelled ST case experiences 38.9% greater heat transfer than the unfuelled ST case, while the unfuelled FL case experiences the least heat transfer. The fuelled FL case encounters similar heat transfer to the unfuelled ST case; however, the split between inlet/combustor of 51/49 differs from the 58/42 split for the unfuelled ST case. Comparing each fuelled simulation, the FL case suffers 27.7% less heat transfer than the ST case. While the 73.73 kW of heat transfer for the FL case exceeds the 31 kW cooling capacity available from the hydrogen fuel, the remaining heat loads may be manageable by other measures. It is noted that, in addition to conduction dispersing heat throughout the airframe (which could be investigated using conjugate heat transfer solvers [38]), RANS-based CFD is known to over predict heat transfer in scramjet engines (when compared to large eddy simulation techniques [44]) and hence, the true heating loads may be lower than those indicated in Table 3.

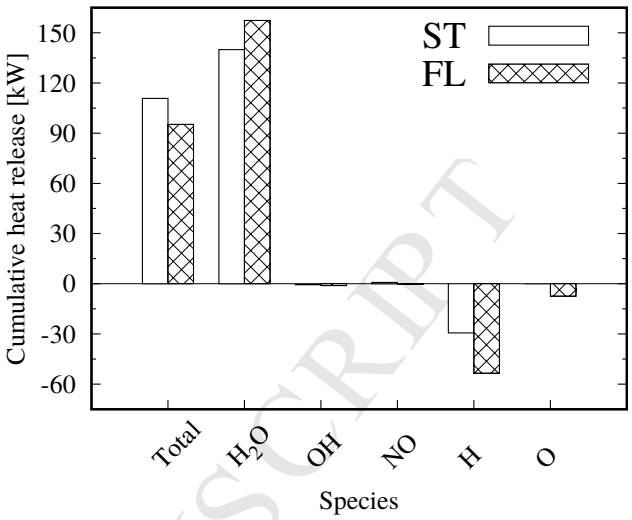

Fig. 9: Species-specific cumulative heat release

Table 3: Heating loads

Flow case	Heat load (kW)			Normalised
	Inlet	Comb.	Total	total
ST unfuelled	42.59	30.83	73.42	1.000
ST fuelled	45.65	56.34	101.99	1.389
FL unfuelled	37.37	28.19	65.56	0.893
FL fuelled	37.88	35.85	73.73	1.004

V 5. Conclusion

The present study numerically compares the performance of a Mach 12, shape-transitioning scramjet when operating under conditions characteristic of impulse facilities, to its performance under steady-flight operation. The flight representative case experienced thickened forebody boundary layers, while the increased fuel temperature improved its jet penetration upon the inlet. Aided by elevated fuel and wall

temperatures, the reduced ignition delay encountered in the flight case induced premature ignition, with significant OH production occurring further upstream than in the shock tunnel case. As the inlet-based fuel injectors were designed for shock tunnel experiments, the flight case may benefit from these injectors being moved further downstream.

Following secondary fuel injection at the combustor, the flight case maintained greater temperatures throughout the combustor. Too high for complete and efficient combustion to proceed, these temperatures impaired the recombination of combustion radicals. Despite improved mixing rates and a greater gross-rate of heat release due to water formation, the high temperatures encountered in the flight case ensured much of this heat was absorbed through the dissociation of reactants. Hence, 16.4% more net-heat was released in the shock tunnel case. However, the increased scramjet wall temperature for the flight case ensured 27.7% less heat was absorbed by the flow path walls. With these counteracting changes in heat release and transfer, these findings suggest that optimal engine design for flight may differ considerably from that which gives the best performance in the tunnel.

6. Funding Sources

This research was undertaken with the assistance of resources provided at the NCI National Facility and the Pawsey Supercomputing Centre through the National Computational Merit Allocation Scheme supported by the Australian Government. Will Landsberg acknowledges support through the Australian Government Research Training Program Scholarship.

7. Acknowledgments

The authors would like to thank Professor Graham Candler's research group for providing their CFD research code.

8. References

[1] Denman, Z., Wheatley, V., Smart, M., and Veeraragavan, A., "Supersonic Combustion of Hydrocarbons in a Shape-Transitioning Hypersonic Engine," *Proceedings of the Combustion Institute*, Vol. 36, No. 2, 2017, pp. 2883–2891. doi:10.1016/j.proci.2016.08.081.

[2] Landsberg, W., Gibbons, N., Wheatley, V., Smart, M., and Veeraragavan, A., "Improving Scramjet Performance Through Flow Field Manipulation," *Journal of Propulsion and Power*, 2017. doi:10.2514/1.B36772, Accessed November 21, 2017.

[3] Stalker, R., Paull, A., Mee, D., Morgan, R., and Jacobs, P., "Scramjets and Shock Tunnels - The Queensland Experience," *Progress in Aerospace Sciences*, Vol. 41, No. 6, 2005, pp. 471–513. doi:10.1016/j.paerosci.2005.08.002.

[4] Hank, J., Murphy, J., and Mutzman, R., "The X-51A Scramjet Engine Flight Demonstration Program," *15th AIAA International Space Planes and Hypersonic Systems and Technologies Conference*, Dayton, Ohio, 2008. doi:10.2514/6.2008-2540.

[5] McClinton, C. R., Rausch, V. L., Shaw, R. J., Metha, U., and Naftel, C., "Hyper-X: Foundation for Future Hypersonic Launch Vehicles," *Acta Astronautica*, Vol. 57, No. 2, 2005, pp. 266–276. doi:10.1016/j.actaastro.2005.03.060.

[6] Smart, M., Hass, N. E., and Paull, A., "Flight Data Analysis of the HyShot 2 Scramjet Flight Experiment," *AIAA Journal*, Vol. 44, No. 10, 2006, pp. 2366–2375. doi:10.2514/1.20661.

[7] Jackson, K., Gruber, M., and Buccellato, S., "HIFiRE Flight 2-A Program Overview," *51st AIAA Aerospace Sciences Meeting including the New Horizons Forum and Aerospace Exposition*, Grapevine, Texas, 2013. doi:10.2514/6.2013-695.

[8] Barth, J. E., Wheatley, V., and Smart, M. K., "Effects of Hydrogen Fuel Injection in a Mach 12 Scramjet Inlet," *AIAA Journal*, Vol. 53, No. 10, 2015, pp. 2907–2919. doi:10.2514/1.J053819.

[9] Wise, D. J., and Smart, M. K., "Experimental Investigation of a Three-Dimensional Scramjet Engine At Mach 12," *20th AIAA International Space Planes and Hypersonic Systems and Technologies Conference*, 2015. doi:10.2514/6.2015-3650.

[10] Ferlemann, P. G., "Hyper-X Mach 10 Scramjet Preflight Predictions Vs. Flight Data," *13th International Space Planes and Hypersonic Systems and Technology Conference*, Capua, Italy, 2005. doi:10.2514/6.2005-3352.

[11] McClinton, C., Rausch, D., Sitz, J., and Reukauf, P., "Hyper-X Program Status," *10th AIAA/NAL-NASDA-ISAS International Space Planes and Hypersonics Systems and Technologies Conference*, Kyoto, Japan, 2001. doi:10.2514/6.2001-1910.

[12] Boyce, R., and Paull, A., "Scramjet Intake and Exhaust CFD Studies for the HyShot Scramjet Flight Experiment," *10th AIAA/NAL-NASDA-ISAS International Space Planes and Hypersonics Systems and Technologies Conference*, Kyoto, Japan, 2001. doi:10.2514/6.2001-1891.

[13] Boyce, R., Gerard, S., and Paull, A., "The HyShot Scramjet Flight Experiment - Flight Data and CFD Calculations Compared," *12th International Space Planes and Hypersonic Systems and Technology Conference*, Norfolk, Virginia, 2003. doi:10.2514/6.2003-7029.

[14] Duan, L., Beekman, I., and P., M. M., "Direct Numerical Simulation of Hypersonic Turbulent Boundary Layers. Part 2. Effect of Wall Temperature," *Journal of Fluid Mechanics*, Vol. 655, 2010, pp. 419–445. doi:10.1017/S0022112010000959.

[15] Cook, R. T., Fryk, E. E., and Newell, J. F., "SSME Main Combustion Chamber Life Prediction," Tech. Rep., 1983. Document ID:19830027830.

[16] Mutzman, R., and Murphy, S., "X-51 Development: A Chief Engineer'S Perspective," *7th AIAA International Space Planes and Hypersonic Systems and Technologies Conference*, 2011. AIAA Key Speech.

[17] Barth, J., "Mixing and Combustion Enhancement in a Mach 12 Shape-Transitioning Scramjet Engine," Ph.D. Thesis, University of Queensland, Brisbane, Queensland, Australia, 2014. doi:10.14264/uql.2014.614.

[18] Smart, M. K., "Design of Three-Dimensional Hypersonic Inlets with Rectangular-To-Elliptical Shape Transition," *Jour-*

nal of Propulsion and Power, Vol. 15, No. 3, 1999, pp. 408–416. doi:10.2514/2.5459.

[19] Doherty, L., Smart, M., and Mee, D., "Experimental Testing of an Airframe-Integrated Three-Dimensional Scramjet At Mach 10," *AIAA Journal*, Vol. 53, No. 11, 2015, pp. 3196–3207. doi:10.2514/1.J053785.

[20] Preller, D., and Smart, M. K., "Reusable Launch of Small Satellites Using Scramjets," *Journal of Spacecraft and Rockets*, Vol. 54, No. 6, 2017, pp. 1317–1329. doi:10.2514/1.A33610.

[21] Nompelis, I., Drayna, T., and Candler, G., "Development of a Hybrid Unstructured Implicit Solver for the Simulation of Reacting Flows Over Complex Geometries," *34th AIAA Fluid Dynamics Conference and Exhibit*, 2004. doi:10.2514/6.2004-2227.

[22] MacCormack, R. W., and Candler, G. V., "The Solution of the Navier-Stokes Equations Using Gauss-Seidel Line Relaxation," *Computers & Fluids*, Vol. 17, No. 1, 1989, pp. 135–150. doi:10.1016/0045-7930(89)90012-1.

[23] Blottner, F. G., Johnson, M., and Ellis, M., "Chemically Reacting Viscous Flow Program for Multi-Component Gas Mixtures," Technical report, Sandia Labs, 1971. OSTI Identifier: 4658539.

[24] Wright, M. J., Candler, G. V., and Bose, D., "Data-Parallel Line Relaxation Method for the Navier-Stokes Equations," *AIAA Journal*, Vol. 36, No. 9, 1998, pp. 1603–1609. doi:10.2514/2.586.

[25] Spalart, P. R., and Allmaras, S. R., "A One-Equation Turbulence Model for Aerodynamic Flows," *30th Aerospace Sciences Meeting and Exhibit, Aerospace Sciences Meetings*, 1992. doi:10.2514/6.1992-439.

[26] Gehre, R. M., Wheatley, V., Boyce, R. R., Peterson, D. M., and Brieschenk, S., "Reynolds-Averaged Navier-Stokes And Wall-Modelled Large-Eddy Simulations of Sonic Hydrogen Injection Into Hypersonic Crossflow," *Proceedings of the 18th Australasian Fluid Mechanics Conference*, 2012.

[27] Gordon, S., and McBride, B. J., "Computer Program for Calculation of Complex Chemical Equilibrium Compositions and Applications. Part 1: Analysis," Tech. Rep., NASA Lewis Research Center, 1994. URL `https://ntrs.nasa.gov/search.jsp?R=19950013764`, NASA Reference Publication 1311.

[28] Jachimowski, C. J., "An Analysis of Combustion Studies in Shock Expansion Tunnels and Reflected Shock Tunnels," Tech. Rep., NASA Langley Research Center, 1992. NTRS: 19920019131.

[29] Stern, F., Wilson, R., Coleman, H., and Paterson, E., "Comprehensive Approach to Verification and Validation of CFD Simulations - Part 1: Methodology and Procedures," *Journal of Fluids Engineering*, Vol. 123, No. 4, 2001, pp. 793–802. doi:10.1115/1.1412235.

[30] Kang, X., Gollan, R. J., Jacobs, P. A., and Veeraragavan, A., "On the Influence of Modelling Choices on Combustion in Narrow Channels," *Computers and Fluids*, Vol. 144, 2017, pp. 117–136. doi:10.1016/j.compfluid.2016.11.017.

[31] Banks, J., Aslam, T., and Rider, W., "On Sub-Linear Convergence for Linearly Degenerate Waves in Capturing Schemes," *Journal of Computational Physics*, Vol. 227, No. 14, 2008, pp. 6985–7002. doi:10.1016/j.jcp.2008.04.002.

[32] Doherty, L. J., Zander, F., Jacobs, P. A., Gollan, R. J., Chan, W. Y., and Kirchhartz, R., "NENZF-r: Non-Equilibrium Nozzle Flow, Reloaded. A User Guide." Tech. Rep., School of Mechanical and Mining Engineering, The University of Queensland, Brisbane, Australia, 2012.

[33] Gardner, A., Paull, A., and McIntyre, T., "Upstream Porthole Injection in a 2-D Scramjet Model," *Shock Waves*, Vol. 11, No. 5, 2002, pp. 369–375. doi:10.1007/s001930200120.

[34] Beyer, S., Schmidt-Wimmer, S., Quering, K., Wilhelmi, C., and M., S., "Technology Status of Fuel Cooled Ceramic Matrix Composites for Dual-Mode Ramjet (DMR) and Liquid Rocket Engine (LRE) Applications," *18th AIAA/3AF International Space Planes and Hypersonic Systems and Technologies Conference*, 2012. doi:10.2514/6.2012-5877.

[35] Wieting, A. R., and Gufi., R. W., "Thermal-Structural Design/Analysis of an Airframe-Integrated Hydrogen-Cooled Scramjet," *Journal of Aircraft*, Vol. 13, No. 3, 1976, pp. 192–197. doi:10.2514/3.58649.

[36] Qin, J., Bao, W., Zhang, S., and Zhou, W., "Comparison During a Scramjet Regenerative Cooling and Recooling Cycle," *Journal of Thermophysics and Heat Transfer*, Vol. 26, No. 4, 2012, pp. 612–618. doi:10.2514/1.T3820.

[37] Leachman, J. W., Jacobsen, R. T., Penoncello, S. G., and Lemmon, E. W., "Fundamental Equations of State for Parahydrogen, Normal Hydrogen, and Orthohydrogen," *Journal of Physical and Chemical Reference Data*, Vol. 38, No. 3, 2009, pp. 721–748. doi:10.1063/1.3160306.

[38] Veeraragavan, A., Beri, J., and Gollan, R. J., "Use of the Method of Manufactured Solutions for the Verification of Conjugate Heat Transfer Solvers," *Journal of Computational Physics*, Vol. 307, 2016, pp. 308–320. doi:10.1016/j.jcp.2015.12.004.

[39] Kovachevich, A., Hajek, K., McIntyre, T., Paull, A., and Abdel-jawad, M., "Imaging of Hydrogen Fuel Injection on the Intake of a Heated Wall Scramjet," *Proceedings of the 42nd AIAA/ASME/SAE/ASEE Joint Propulsion Conference & Exhibit*, Sacramento, CA, 2006. doi:10.2514/6.2006-5039.

[40] Kutschenreuter, P., *Scramjet Propulsion: Supersonic Flow Combustors*, American Institute of Aeronautics and Astronautics, Inc., 2000. doi:10.2514/5.9781600866609.0513.0568.

[41] Turns, S. R., *An Introduction to Combustion: Concepts and Applications*, 3rd ed., McGraw-Hill, 2000.

[42] Smart, M., "How Much Compression Should a Scramjet Inlet Do?" *AIAA Journal*, Vol. 50, No. 3, 2012, pp. 610–619. doi:10.2514/1.J051281.

[43] Landsberg, W., Wheatley, V., and Veeraragavan, A., "Characteristics of Cascaded Fuel Injectors Within an Accelerating Scramjet Combustor," *AIAA Journal*, Vol. 54, No. 12, 2016, pp. 3692–3700. doi:10.2514/1.J054815.

[44] Fureby, C., Chapuis, M., Fedina, E., and Tegnér, J., "A Computational Study of Scramjet Combustion," *27th International Congress of the Aeronautical Sciences*, Nice, France, 2010.

- Scramjets experience heating loads in flight, raising engine wall temperatures
- Operation under both shock tunnel and flight conditions is compared numerically
- Inlet fuel injection promotes mixing, but triggers premature ignition in flight
- Reduced combustion heat release and loss to the walls is encountered in flight
- Optimal flight engine design may differ greatly from optimal shock tunnel design